

Staring array sensor model for simulation implementation

Cornelius J. Willers^a and Maria S. Willers^b

^aAirbus DS Optronics (Pty) Ltd, Nellmapius Drive, PO Box 8859, Centurion 0046, South Africa

^bDenel Dynamics, P.O. Box 7412, 0046 Centurion, South Africa

ABSTRACT

A comprehensive model for staring array simulation is described. The model covers all effects from photon signal generation through to detection and processing in the staring array sensor. The model follows the signal flow from photon generation, through a staring focal plane array (FPA) from the detector, through several conversions in the read out integrated circuit (ROIC) and finally conversion to a digital signal. Spatial nonuniformity modeling for photoresponse, dark current generation and source follower offset is included. The list of noise sources includes: photon noise, quantum conversion uncertainty, dark noise, kTC noise, source follower noise and quantization noise. Several components with (simplified) nonlinear responses are also modeled: sense node capacitance variation with charge, source follower nonlinearity and nonlinearity in the digital conversion. The code implementations take images as input, applying the various processes independently on individual pixels (e.g., shot noise) or on complete images (e.g., spatial nonuniformity). Some noise sources vary temporally across frames (shot, thermal, kTC) while other noise sources are fixed across frames (fixed pattern noises). The application of the model is demonstrated by tracing the signal path from source to sensor output, with intermediate results along the path. The model is implemented in Python (as part of the pyradi open source computational radiometry module) and in a C++ image simulation. The purpose with this work is to predict what the performance of a given sensor will be in terms of image appearance, given the devices specifications and key design parameters. The execution of this work lead to the important recommendation that nonuniformity correction for infrared sensors should be performed at well fill levels corresponding to the minimum and maximum in the scene, not to fixed percentage levels in the charge well.

The objective with this work is to provide a ‘generic’ model that can be adapted by adjusting model parameters. For more accurate modeling of specific sensors, dedicated models should be developed, but for all but the most demanding requirement, this model should be adequate in scope of detail and freedom of characteristics.

Keywords: staring array performance, image simulation, photoresponse nonuniformity (PRNU), focal plane array (FPA)

1. INTRODUCTION

1.1 Overview

This paper describes a comprehensive system-level staring array sensor model for application in the visible and infrared spectral ranges. The purpose with this work is to predict what the performance of a given sensor will be in terms of image appearance, given the devices specifications and key design parameters. The model has been used for performance prediction and design optimization of visual and infrared sensors. The model accounts for all significant noise sources and processing artifacts in the detector array and ROIC. The model supports low photon-count (low light) scenarios and high photon-count infrared scenarios. The work described in this paper is based in part on the ‘Photon Transfer’ model described by Janesick,¹ which inspired an expanded Matlab implementation by Konnik.² A Python implementation, available in the pyradi library³ expands on Konnik’s work. This expanded model is also implemented in C++ image simulation system.⁴

The model follows the signal flow from photon generation, through a staring FPA from the detector, through several conversions in the ROIC and finally conversion to a digital signal. Spatial nonuniformity modeling for

Further author information: (Send correspondence to C.J.W.)

C.J.W.: E-mail: neliswillers@gmail.com, Telephone: +27-83-259-0033

M.S.W.: E-mail: riana.willers@deneldynamics.co.za, Telephone: +27-12-671-1901

photoresponse, dark current generation and source follower offset is included. The list of noise sources includes: photon noise, quantum conversion uncertainty, dark noise, kTC noise, source follower noise and quantization noise. Several components with (simplified) nonlinear responses are also modeled: sense node capacitance variation with charge, source follower nonlinearity and nonlinearity in the digital conversion. Inter-pixel effects such as optical MTF, detector crosstalk, and diffusion MTF are assumed already accounted for in the photon rate image, prior to the application of this model.

The code implementations take images as input, applying the various processes independently on individual pixels (e.g., shot noise) or on complete images (e.g., spatial nonuniformity). Some noise sources vary temporally across frames (shot, thermal, kTC) while other noise sources are fixed across frames (fixed pattern noises).

The objective with this work is to provide a ‘generic’ model that can be adapted by adjusting model parameters. For more accurate modeling of specific sensors, dedicated models should be developed, but for all but the most demanding requirement, this model should be adequate in scope of detail and freedom of characteristics. The model is readily applied to sensors with CMOS ROIC operating in the short wave infrared (SWIR 1–2.5 μm), medium wave infrared (MWIR 3–5 μm), and long wave infrared (LWIR 8–12 μm) spectral bands by appropriate parameter definitions.

2. MODEL DESCRIPTION

2.1 Read out technologies

Modern digital focal array plane detectors employ (1) an array of detectors to capture the photons and convert them to electrons, and (2) a read out mechanism (ROIC) to transform the detector signal into a serial data stream. The ROIC can use either a charge coupled device (CCD) or a complementary metal oxide (CMOS) technology to read out the detector signal. Visual band sensors use silicon technology for detection and use either CCD or CMOS ROIC (all functionality in a monolithic chip). Infrared sensors use silicon CMOS ROIC, but one of many different detector materials. The detector chip and ROIC chip are interconnected most often with indium bumps on chip level (hybrid technology). Figure 1 presents a comparison of the commonality and differences between the CCD and CMOS technologies. Photon capture in the material, its conversion to electrons and the accumulation of electrons are performed by a two-dimensional array of detector devices. Each pixel accumulates charge on a capacitor within the footprint of the detector pixel itself. CCD and CMOS differ in the methods used to store, move and read out the signals. CCD devices transfer charges along its two-dimensional structures, whereas CMOS devices keep charges local and make voltage levels available in its two-dimensional structures.

In the case of CCDs, the two-dimensional array of charges are transferred along one axis (say x) to the edge of the array, where another charge transferring mechanism moves the charges along the other axis (say y) via a readout node to the outside world. The CCD’s readout node performs the charge to current conversion. There are only a small number of readout nodes (one to eight) where this conversion takes place. Charge accumulation under each pixel, charge transfer and eventual charge conversion are all (approximately) linear processes. There may be differences in gain and offset between the different charge transfer and conversion channels, exhibiting as spatial nonuniformity.

In the case of CMOS, the charges are collected in a two-dimensional array of charge well capacitors, converted to voltages at each detector pixel, and the voltage at each pixel is read out by multiplexed switches of each detector signal to the outside world. The charge accumulation in the CMOS device may be nonlinear and the gain and offset variations all appear at pixel level, but there may be some spatially structured variations attributable to differences between different readout channels.

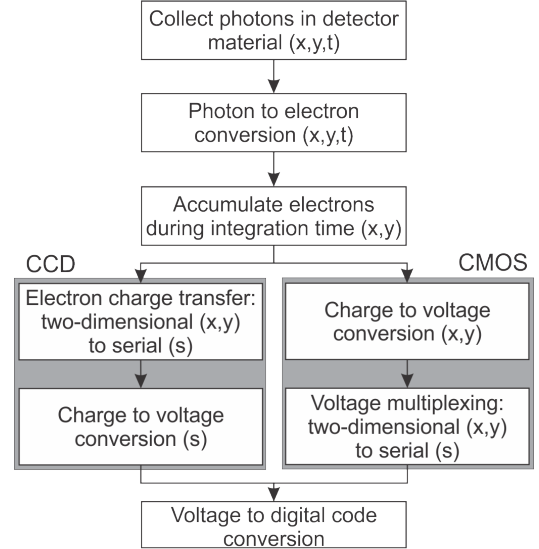


Figure 1: CMOS and CCD FPA detectors compared (adapted⁵).

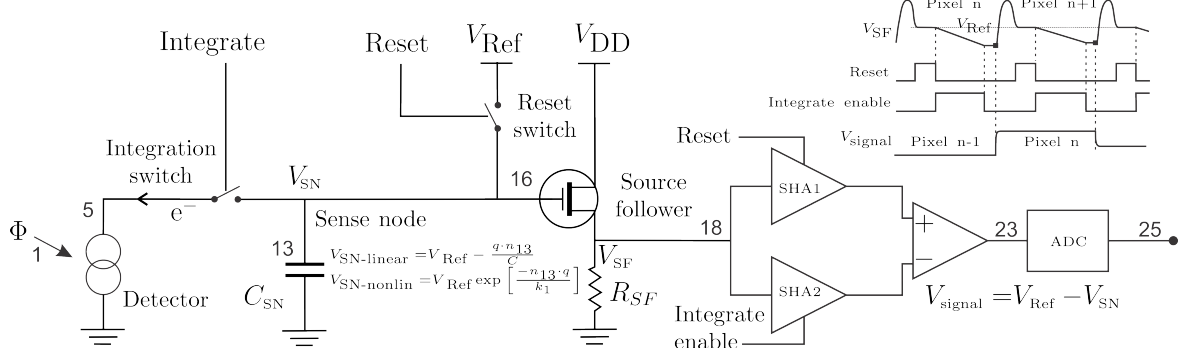


Figure 2: Simplified sensor concept diagram, adapted.^{1,6}

2.2 High-level staring array sensor model

Modeling the two different ROIC technologies require different approaches because of the inherent differences in charge and voltage processing. However, with some poetic licence and appropriate parameter selection it is possible to use a single model for high-level image simulation. The model presented here has a hybrid CMOS/CCD structure, with switchable options. CMOS ROIC designs have a large number of different topologies,⁷ ranging from simple voltage follower at each detector (as is used in CCD ROICs), direct injection (DI), buffered direct injection (BDI), capacitive transimpedance amplifiers (CTIA), and gate modulated input (GMI) circuits. Circuit complexity can range from a few transistors to many transistors per pixel (designated as e.g., 3T, 5T, etc.). This model uses a source follower topology in order to model both CCD and CMOS devices.

Figure 2 shows a simplified diagram illustrating typical focal plane array processing. Real devices have much more complicated circuitry, containing patented techniques. The photoelectron current is integrated in the charge well capacitor for a specified integration time period t_{int} (synchronized with the data clock). The charge well capacitor may or may not be the actual detector junction capacitance. The charge well capacitor (C) accumulates charges, but in the process also provides a voltage (V) signal proportional to the charge (Q), by $Q = CV$, hence $V = Q/C$. The charge well capacitance exists in a semiconductor device and hence the capacitance depends on the voltage across the capacitor: the transfer function from charge to voltage may therefore be nonlinear $V = Q/C(V)$ in some devices. The charge well has a finite charge capacity, constrained by the well capacitance and the allowable maximum signal voltage range. Prior to the integration time start the charge well capacitor is reset to a nonzero reference voltage V_{Ref} (a value around 2 to 3 V), and during integration the capacitor is discharged from V_{Ref} to some lower value closer to zero. The signal is the change in voltage from the initial V_{Ref} . The correlated double sampling (CDS) circuit employs two sample and hold amplifier (SHA) circuits to eliminate pixel-to-pixel reference voltage offset differences. During pixel value reset, prior to the integration period, the first SHA samples the pixel reset voltage. The second SHA samples the pixel voltage after integration. The CDS circuit measures the difference between the two SHAs, thereby removing the effect of V_{Ref} differences between pixels.

The model accepts an input image in photon rate irradiance [$q/(s \cdot m^2)$] in the detector plane and then proceeds to calculate the various noise components and signal components along the signal flow chain. The signal chain is depicted in Figure 3. The captured photoelectron charge in the detector is determined by the irradiance on the detector, the detector quantum efficiency, detector area and integration time. The photoelectron charge is converted to a voltage in the sense node, is further processed and finally converted to a digital count.

Many noise sources contribute to the resulting noise image produced by the sensor. Noise sources can be broadly classified as either *fixed-pattern* (spatially stable, time invariant) or *temporal* (time-variant) noise. Fixed-pattern noise refers to any spatial pattern that does not change significantly from frame to frame. Temporal noise, on the other hand, changes from one frame to the next. All these noise sources are modeled in various blocks in the signal chain. Different noise sources have different noise statistics. Noise power from multiple uncorrelated noise sources adds in quadrature (noise variance adds linearly). However, at specific moments in

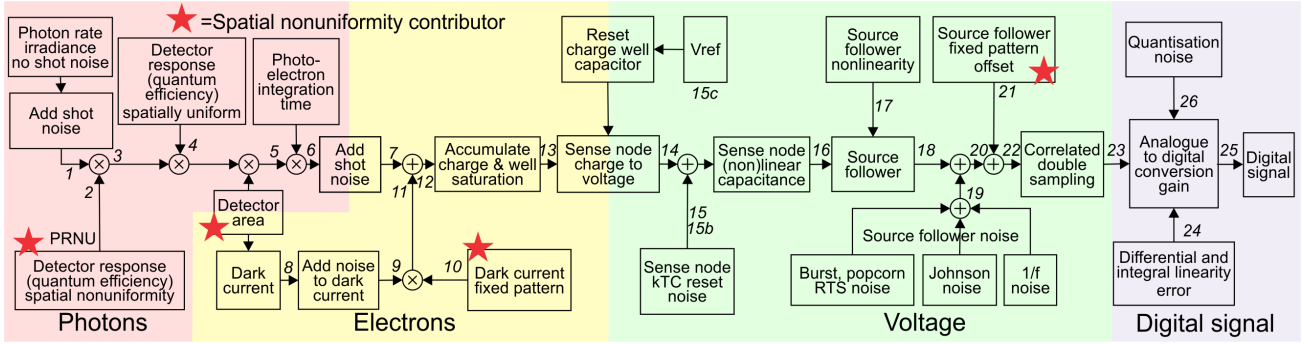


Figure 3: Sensor model elements, expanded.²

$$n = \left(\frac{\pi t_{\text{int}} P A_{\text{det}}}{4F_{\#}^2} \right) \int_0^{\infty} d\lambda \begin{bmatrix} \text{Thermal flux} \\ \underline{S} \underline{S} \underline{S} \underline{A} \underline{T} \underline{T} \\ (\eta_{\lambda} \tau_{\lambda o} \tau_{\lambda f} \tau_{\lambda a}) (\epsilon_{\lambda} L_{\lambda} (T_{\text{source}})) \\ \dots \\ \text{Reflected flux} \\ \underline{S} \underline{S} \underline{S} \underline{S} \underline{T} \underline{T} \\ (\eta_{\lambda} \tau_{\lambda o} \tau_{\lambda f} \tau_{\lambda a}) (\cos \theta \rho_{\lambda d} [\psi L_{\lambda} (T_{\text{illum}})]) \\ \dots \\ \text{Not modelled} \\ \underline{S} \underline{S} \underline{S} \underline{A} \underline{A} \\ (\eta_{\lambda} \tau_{\lambda o} \tau_{\lambda f}) L_{\lambda \text{path} \infty} (1 - \tau_{\lambda \text{path}}) \\ \dots \\ \text{Atmospheric path} \\ \underline{S} \underline{S} \underline{S} \underline{A} \underline{A} \\ (\eta_{\lambda} \tau_{\lambda o} \tau_{\lambda f}) L_{\lambda \text{path} \infty} (1 - \tau_{\lambda \text{path}}) \end{bmatrix}$$

All these terms are summed together inside the spectral integral

Figure 4: Photoelectron generation model.

time the instantaneous (sampled) noise magnitudes add linearly with the signal to yield the total signal at that instant.

The projected optics f-number solid angle is given by $\Omega_f = \pi \sin^2 \theta = \pi(\text{NA})^2 = \pi/(2F_{\#})^2$ where θ is the half apex angle of the f-number cone, NA is the optics' numerical aperture, and $F_{\#}$ is the f-number at infinite conjugates. The well fill is calculated from the signal and integration time as follows:

$$n_f = \eta \Phi_{\text{det}} t_{\text{int}} = \eta E_{\text{det}} \Omega_f t_{\text{int}} = \eta L_{\text{det}} A_d \Omega_f t_{\text{int}} = \eta L_{\text{det}} A_d \pi t_{\text{int}} / (2F_{\#})^2 = \pi t_{\text{int}} A_d \eta L_{\text{det}} / (2F_{\#})^2 \quad (1)$$

where n_f is the electron count well fill, η is the detector quantum efficiency, Φ_{det} is the photon rate flux onto the detector in [q/s], t_{int} is the integration time in [s], E_{det} is the photon rate irradiance in the detector plane in [q/(s.m²)], L_{det} is the photon rate radiance at the detector in [q/(s.m².sr)], and A_d is the area of the detector in [m²]. This well fill may be saturated in the hardware by the finite available voltage swing on the charge well capacitor. Radiant radiometric unit values should be converted to photon units by accounting for the energy of a photon $h\nu = hc/\lambda$, where h is Planck's constant [Js], ν is frequency [Hz], c is the speed of light [m/s], and λ is the wavelength [m].

2.3 Photon rate signal outside the sensor (Node 1)

The sensor model does not include the creation of an input photon rate image, this should be done externally. A comprehensive model^{8,9} should include all the contributions shown in Figure 4. The total electron count in the detector is given by the sum of all the terms defined in Figure 4, where the underlined T , A , and S signifies the origin of the contribution (Target, Atmosphere, and Sensor). The terms in Figure 4 are t_{int} the integration time [s], P is the fraction of clear aperture [-], A_d is the detector area [m²], $F_{\#}$ is the f-number [-], η_{λ} is the detector quantum efficiency [-], $\tau_{o\lambda}$ is the optics transmittance [-], $\tau_{f\lambda}$ is the sensor filter transmittance [-], $\tau_{a\lambda}$ is the atmospheric transmittance [-], ϵ_{λ} is the source/background emissivity [-], $\epsilon_{\text{optics}\lambda} = (1 - \tau_{o\lambda})$ [-], $L_{\lambda}(T)$ the Planck photon rate radiance [q/(s.m².sr)] at temperature T [K], θ is the angle [rad] between the surface normal vector and the primary source (if not the sun or the moon, $\theta = 0$), $\rho_{d\lambda}$ is the surface's diffuse spectral reflection

$[-], \psi = A_{\text{illum}}/(\pi R_{\text{illum}}^2)$ [sr/sr] relating the illuminator radiometry to the target⁹ (for the sun $\psi = 2.17 \times 10^{-5}$), T_{source} is the temperature of the object [K], T_{illum} is the temperature of the illuminating source [K], and path radiance at one range can be scaled to path radiance at another range. It can be shown⁹ that for homogeneous paths, the path radiance can be approximated by $L_{\lambda\text{path}} = L_{\lambda\text{path}\infty}(1 - \tau_{\lambda\text{path}})$ where $L_{\lambda\text{path}\infty}$ is the path radiance for an infinitely long path where $\tau_{\lambda\text{path}} = 0$. More details are available in the pyradi example notebook 09b.¹⁰ The creation and arrival of a photon stream is a series of discrete events (Poisson statistics) and is subject to Bose-Einstein statistics where the noise variance is given by

$$\sigma_{\Phi}^2 = \Phi \frac{\exp(h\nu/kT)}{\exp(h\nu/kT) - 1}, \quad (2)$$

where Φ is the mean value flux [q/s], h is Planck's constant [Js], ν is the flux frequency [Hz], k is Boltzmann's constant [J/K], and T is the temperature [K]. At wavelengths below 15 μm and temperatures lower than 300 K, $h\nu \ll kT$ and the photon noise equation simplifies to $\sigma_{\Phi}^2 = \Phi$. Photon noise has no spatial structure (other than the differences between flux levels in adjacent pixels) and is random across subsequent image frames.

2.4 Processes in the sensor

2.4.1 Detector fixed pattern noise; quantum efficiency spatial nonuniformity (Nodes 2 and 3)

Fixed pattern noise¹⁴ (FPN) is the temporally constant spatial variation between pixels in the FPA output under uniform illumination. It is caused by photo response nonuniformity (PRNU), arising from spatial variations in the individual pixel's responsive area, spectral quantum efficiency or some other responsive characteristic. FPN is proportional to the input flux and is hence expressed as a percentage of input flux. Typical values are $\sigma_{\text{PRNU}}=0.01$ to 0.05 for visual band silicon detectors, 0.05 to 0.15 for SWIR detectors, and 0.2 to 0.3 for MWIR detectors. The PRNU for SWIR and MWIR sensors usually require correction to less than 30% of the sensor's noise equivalent temperature.¹⁵ The signal *after PRNU degradation* is given by (expressed here as flux)

$$\Phi_4 = \Phi_2 [1 + \mathcal{N}(0, \sigma_{\text{PRNU}}^2)] = \Phi_2 \mathcal{N}(1, \sigma_{\text{PRNU}}^2), \quad (3)$$

where $\mathcal{N}(M, \sigma^2)$ is a normal distribution with mean M and variance σ^2 , where each pixel extracts a different sample from the normal distribution. The spatial pattern is constant across subsequent image frames.

Fano noise^{11–13} arises from statistical variation in the photon-to-electron conversion interactions in the detector. It is important for regimes with very low photon count. Fano noise sets the limit for ultra-low noise CCD and CMOS sensors,¹ but is not modeled here.

2.4.2 Detector quantum efficiency (Node 4)

The detector quantum efficiency^{1,9} η is the *mean over all pixels* of the ratio of photogenerated electrons to incident photons over all pixels (spatial variation is already included in the PRNU above). Quantum efficiency comprises two parts: external (fraction of photons entering the detector material) and internal (fraction of photons that entered the material that is eventually converted to photoelectrons). The mean quantum efficiency is given by⁹

$$\eta_{\lambda} = (1 - \rho_{\lambda})(1 - e^{-\alpha_{\lambda}d}), \quad (4)$$

where ρ_{λ} is the spectral semiconductor Fresnel reflectance, α_{λ} is the spectral detector material absorption coefficient, and d in [m] is the depth over which absorption takes place in the material (i.e., depth of the active region in the detector). It is evident that the quantum efficiency increases when the reflectance decreases or where the absorption thickness $\alpha_{\lambda}d$ is high.

2.4.3 Detector area and integration time (Nodes 5 and 6)

Detector pixel area A_d and integration time t_{int} are represented by simple scalar values on the assumption of constant area and integration time across all detector pixels. Variations in detector area are already accounted for in the PRNU (Section 2.4.1). Variations in integration time between different pixels are considered negligible because of a common time base between all pixels.

Table 1: Dark current model coefficients¹⁰ (Equation 5).

Material	e_d	c_a	D_X	T_X	$E_{\text{gap}0}$	A	B
Silicon (visual)	2	4.31×10^5	5.00×10^{-6}	300	1.166	5.50×10^{-4}	636
InGaAs x=0.45 1.7 um	1	2.82×10^8	8.53×10^{-5}	300	0.700	5.40×10^{-4}	1076
HgCdTe x=0.304 MWIR	2	2.78×10^4	2.00×10^{-6}	80	0.235	3.00×10^{-4}	500
HgCdTe x=0.225 LWIR	1	9.25×10^4	1.00×10^{-1}	80	0.131	3.00×10^{-4}	200
	-	$\text{K}^{-3/2}$	A/m^2	K	eV	-	-

2.4.4 Detector electron count shot noise (Node 7)

The arrival of electrons in the charge well is a series of discrete events with Poisson statistics with variance equal to the mean signal $\sigma_{n_f}^2 = \langle n_f \rangle$. Shot noise has no spatial structure and is temporally random in each pixel across subsequent image frames. This model deviates significantly from Konnik's model in that Konnik calculates the shot noise only for the photon flux (Section 2.3) and not for the photon-detection events in the detector. This model also calculates the shot noise on the electrons in the charge well. This has an appreciable effect on the final signal to noise ratio.

2.4.5 Dark current, dark shot noise and fixed pattern noise (Nodes 8 to 11)

Dark current flows in a detector with no photon incidence, resulting from many different processes in a detector.^{1,16} Sources of dark current include (depending on the material type and operating temperature): thermal diffusion current, thermal generation and tunneling through bandgap states in the depletion region, and surface current.¹⁶ This very simple model assumes that one of the dark current contributors, diffusion or depletion, is dominant (which may not always be the case), and does not account for reverse bias voltage variations. It appears that the fill factor does not apply to dark current. Combining information from several sources,^{1,10,16–18} the following simple model for the mean dark current signal in electron count is used

$$n_8 = n_{\text{darkcurrent}} = (t_{\text{int}}/q) I_{\text{D-A}}(T, A_d) = (t_{\text{int}}/q) c_a D_X A_d T^{3/2} \exp(-E_{\text{gap}}/(e_d k T)), \quad (5)$$

where q is the charge on an electron, A_d is the pixel detector area [m^2], t_{int} is the integration time, $I_{\text{D-A}}(T, A_d)$ is the dark current in A, c_a is a material-dependent temperature compensation factor^{10,17} calculated at temperature T_X , D_X is the dark current density in A/m^2 (paired with c_a at temperature T_X), T is the detector temperature in K, e_d is a constant according to the dominant dark current process, and $k = 8.617 \times 10^{-5}$ eV/K is Boltzmann's constant in electron volt units. The material band gap E_{gap} temperature variation is approximated by the Varshni model

$$E_{\text{gap}}(T) = E_{\text{gap}0} - \frac{A T^2}{T + B}. \quad (6)$$

The parameter values for Equation 5 are shown in Table 1. The dark current carriers create a temporal electron count shot noise (Poisson distributed) with variance $\sigma_{\text{dark}}^2 = n_{\text{darkcurrent}}$. The dark current noise σ_{dark} is random over pixels and subsequent image frames.

The dark current varies between pixels but is constant for each pixel over time, causing a spatial noise called dark current fixed pattern noise (DFPN). The DFPN is not the same as the PRNU for photoelectron generation (Section 2.4.1), it is caused by different processes, has a different statistical nature, and has a much wider variation. Konnik argues² for a multi-distribution model combining lognormal with other distributions. Konnik's model was verified using experimental work on astronomical cameras, requiring really long integration times. For the present model, only a single lognormal is used to obtain the required 'outlier' or 'hot' noisy dark pixels (alternatively a normal distribution can also be used in the software)

$$n_{11} = n_9 [1 + \log \mathcal{N}(0, \sigma_{\text{DNU}}^2)] = n_9 \log \mathcal{N}(1, \sigma_{\text{DNU}}^2), \quad (7)$$

where $\log \mathcal{N}(M, \sigma_{\text{DNU}}^2)$ is a lognormal probability distribution with mean value M and variance of σ_{DNU}^2 . The dark current nonuniformity standard deviation σ_{DNU} is between 0.1 and 0.4 for silicon detectors¹ and assumed similar for other detector types.

2.4.6 Well saturation and sense node charge to voltage conversion (Nodes 13, 14 and 16)

The sense node is the final collecting point at the end of the readout register of a CCD sensor; the CCD nonlinearity is small ($\leq 0.2\%$, $C = Q/V \approx c$). Each pixel in a CMOS device has its own charge well capacitor; where the voltage dependent capacitance nonlinearity $C(V) = Q/V \neq c$ may be significant, up to 200% for some designs.¹ The V/e^- nonlinearity affects the signal differently from the noise components.¹

For a simple charged capacitor with *fixed capacitance* (e.g. CCD) the voltage is inversely proportional to the capacitance $V = Q/C$. For a fixed sense node capacitance of the order of 20 fF, the sense node gain will be $A_{SN} = q/C_{SN} = 8 \mu\text{V}/\text{e}^-$. The signal voltage (deviation from reference voltage) is then $V_{signal} = n_{13}A_{SN}$. The sense node voltage is

$$V_{SN} = V_{Ref} - n_{13}A_{SN} = V_{Ref} - \frac{q \cdot n_{13}}{C}. \quad (8)$$

Some electronics configurations result in a *variable capacitance*, where the capacitance changes with applied voltage. In the CMOS configuration shown in Figure 2, where the signal grows negatively from the reference voltage, the voltage on the capacitor is not linearly proportional to the photoelectron charge. Assuming that the capacitance is inversely proportional to the voltage on the capacitor,¹ $C_{SN}(V_{SN}) = k_1/V_{SN}$. The solution can be found by solving the equation

$$\frac{dn_{13}}{dV_{SN}} = \frac{C_{SN}(V_{SN})}{q} = \frac{k_1}{qV_{SN}}, \quad (9)$$

where n_{13} is the accumulated charge in electrons, V_{SN} is the voltage on the sense node capacitor, $C_{SN}(V_{SN})$ is the sense node capacitance (a function of the sense node voltage), q is the charge on an electron. Solving the differential equation, given the appropriate boundary values, yields

$$n_{13} = \frac{k_1}{q} \int_{V_{SN}}^{V_{Ref}} \frac{1}{V_{SN}} dV_{SN} = \frac{k_1}{q} \log_e \left[\frac{V_{Ref}}{V_{SN}} \right] = \frac{k_1}{q} \log_e \left[\frac{V_{Ref}}{V_{Ref} - V_{signal}} \right], \quad (10)$$

where the voltage on the charge well capacitor is $V_{SN} = V_{Ref} - V_{signal}$. Then the signal voltage (deviation from reference voltage) is given by

$$V_{signal} = V_{Ref} \left(1 - \exp \left[\frac{-n_{13} \cdot q}{k_1} \right] \right), \quad (11)$$

and the sense node voltage is given by

$$V_{SN} = V_{Ref} \exp \left[\frac{-n_{13} \cdot q}{k_1} \right]. \quad (12)$$

Konnik² introduces an additional nonlinearity factor α , but this has no meaning other than to scale the value of k_1 , so better then change k_1 directly. Janesick's Example 7.2 uses a value $k_1 = 10.909 \times 10^{-15}$, resulting in a capacitance of 4 fF at 3 V and 20 fF at 0.5 V bias on the capacitor. Note that if the nonlinear capacitance follows the inverse-voltage relationship the full well capacity must be calculated using Equation 12 with the minimum sense node voltage (typically around 0.5 V). Note furthermore that the nonlinear capacitance conveniently provides high gain for small signals and a lower gain (compression) for large signals.

2.4.7 Reference voltage and sense node kTC reset noise (Node 15)

At the start of the integration period, the voltage on the sense node capacitor is set to some value V_{Ref} (typically around 3 V), from which increased photoelectron charge reduces the voltage towards a lower value (typically 0.5 V). kTC noise is essentially thermal noise filtered by the presence of a capacitor. When sampling thermal noise the high frequency content of the noise power spectral density (PSD) is aliased to low frequencies. Integrating over all frequencies it can be shown that the sampled noise voltage is given by¹⁹ $\sigma_{kTC-V}^2 = kT/C$ where C is the capacitance holding the sampled signal. Using $Q = CV = nq$ the noise in *electron count* is then given by

$$\sigma_{kTC-n} = \frac{\sqrt{k_B T C_{SN}}}{q} = \sqrt{\frac{k_B T}{q A_{SN}}}, \quad (13)$$

where q is the charge on an electron [C], k_B is the Boltzmann constant [J/K], T is the temperature [T], and $C_{SN} = q/A_{SN}$ is the sense node capacitance [F]. In CCD sensors the sense node reset noise is removed by CDS. In CMOS photo sensors it is difficult to remove the reset noise even after application of CDS. The noise distribution depends on the sensor's architecture and the reset technique; some devices perform hard reset and others soft reset.^{20,21} Soft reset configurations have lower kTC noise (by a factor of $1/\sqrt{2}$ or even less). An inverse gaussian (Wald) distribution can be used to simulate hard-reset kTC noise, and the lognormal distribution can be used for soft-reset kTC noise.² This code presently only implements a lognormal model.

2.4.8 Source follower gain and nonlinearity (Nodes 17 and 18)

The source follower voltage tracks the sense node voltage, providing a high impedance unity gain buffer to prevent discharging of the charge well. At low frequencies, the source follower has a voltage gain

$$A_{SF} = \frac{g_m R_{SF}}{g_m R_{SF} + 1} \approx 1 \quad \text{if } g_m R_{SF} \gg 1 \quad (14)$$

where g_m is the source follower field-effect transistor (FET) transconductance, and R_{SF} is the source resistor. The nonlinear source follower gain, different from Konnik's form,² is given by

$$A_{SFnl} = A_{SF} \left[1 - (\gamma - 1) \left(\frac{V_{Ref} - V_{SN}}{V_{Ref} - V_{Full\ well}} \right) \right], \quad (15)$$

where A_{SFnl} is the nonlinear source follower gain [V/V], A_{SF} is the linear (ideal) source follower gain [V/V], γ is the nonlinear error (typically 0.95 to 1.05) [-], $V_{Full\ well}$ is the voltage [V] on the charge well when filled to capacity, V_{Ref} is the reference voltage [V], and V_{SN} is the sense node voltage [V].

2.4.9 Source follower noise (Node 19)

Pixel-level noise in the source follower consists of three types of noise: (1) white noise, (2) flicker noise, and (3) random telegraph signal (RTS) noise. In CCD photosensors, source follower noise is typically limited by the flicker noise. In CMOS photosensors, source follower noise is typically limited by the RTS noise.

Johnson noise: The output impedance of the source-follower amplifier generates spectrally flat (white) Johnson (thermal) noise as determined by $N_{Johnson}(V_{SF}) = \sqrt{4k_B T B R_{SF}}$ (in volts), where k_B is Boltzmann's constant [J/K], T is temperature [K], B refers to the noise power bandwidth [Hz], and R_{SF} is the resistive component of the source follower output impedance.

Flicker (1/f) noise: Flicker noise originates from material and process imperfections and the existence of silicon-oxide trap states in the image sensor silicon that turn on and off randomly according to different time constants. The flicker noise power spectral density is inversely proportional to frequency, up to the 1/f corner or knee frequency, beyond which the spectrally flat noise floor starts to dominate. The flicker noise often dominates in sensors with low (< 1 MHz) readout speed. For the typical MOSFET amplifiers, the white noise floor occurs at approximately 5 nV/ $\sqrt{\text{Hz}}$.

Random Telegraph Signal (RTS) noise: As the CCD and CMOS pixels are shrinking in dimensions, the low-frequency noise increases. In such devices, the low-frequency noise performance is dominated by Random Telegraph Signals (RTS) on top of the 1/f noise. The origin of such an RTS is attributed to the random trapping and de-trapping of mobile charge carriers in traps located in the oxide or at the interface. The RTS is observed in MOSFETs as a fluctuation in the drain current. A pure two-level RTS is represented in the frequency domain by a Lorentzian spectrum.

The source follower (assumed gaussian) noise variance is calculated using^{1,2}

$$\sigma_{SF} = \frac{\sqrt{\int_0^{\infty} S_{SF}(f) H_{CDS}(f) df}}{A_{SF} [1 - \exp(-t_s/\tau_D)]}, \quad (16)$$

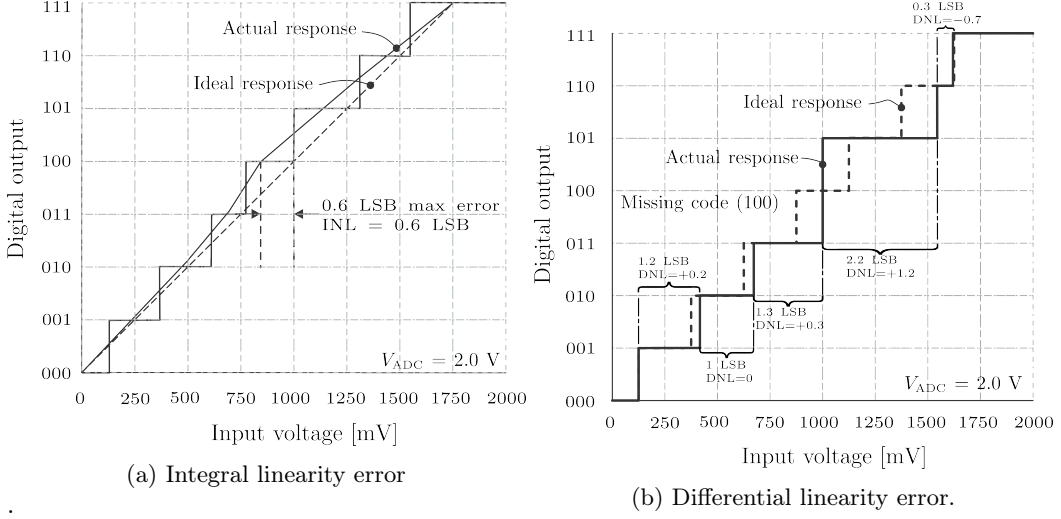


Figure 5: Digital conversion linearity error.²⁴

where σ_{SF} is the source follower noise [volts rms], f is the electrical frequency [Hz], t_s is the CDS sampling interval [s], and $\tau_D = t_s/2$ [s] is the CDS dominant time constant.²² $H_{CDS}(f)$ is the CDS transfer function¹

$$H_{CDS}(f) = \frac{2[1 - \cos(2\pi f t_s)]}{1 + (2\pi f \tau_D)^2}, \quad (17)$$

where the numerator is the CDS processor frequency response and the denominator is the white noise spectrum defined by the sampling frequency. The source follower's noise power spectrum can be described as

$$S_{SF}(f) = W(f)^2 \cdot \left(1 + \frac{f_c}{f}\right) + \frac{2\Delta I^2 \tau_{RTS}}{4 + (2\pi f \tau_{RTS})^2}, \quad (18)$$

where $W(f)$ is the Johnson thermal noise, typically $15 \text{ nV}/\sqrt{\text{Hz}}$, f_c is the flicker noise corner frequency [Hz]. The last term represents RTS noise with τ_{RTS} the RTS characteristic time constant [s], and ΔI the source follower current modulation induced by RTS [A].

2.4.10 Fixed pattern offset and CDS (Nodes 21 and 23)

The electronics readout signal paths for CMOS sensors include several amplifiers, some of which are shared, and some not.²³ The fixed pattern offset for a CCD is assumed zero. In CMOS detectors the variations in column amplifier offsets and gains cause line-structured (column) noise, which is very different from the gaussian noise observed in CCD sensors. Correlated double sampling partly removes offset variations, but cannot remove gain variations. CMOS sensor modeling therefore requires column-to-column variation modeling. The El Gamal²³ fixed pattern offset model includes a first order autoregressive random field calculated *per pixel*, added to another first order autoregressive random field calculated *per column*. El Gamal argues that a first order model is sufficient. Column fixed pattern offset is modeled by the regression

$$Y_j = a(Y_{j-1} + Y_{j+1}) + U_j, \quad (19)$$

where U is $\mathcal{N}(0, \sigma_U^2)$, and $0 \leq a \leq 0.5$ characterizes the dependency of Y_j on its two neighboring columns. El Gamal investigates four different CMOS architectures experimentally and finds that CDS designs have $0.09 \leq a \leq 0.11$ and circuits without CDS has $0.05 \leq a \leq 0.15$ under 70% uniform well fill, and somewhat lower under dark conditions. The current CDS model is a unity gain, zero offset process.

2.4.11 Analog to digital conversion (Nodes 24 to 26)

An N -bit analogue-to-digital converter (ADC) transforms a voltage signal into 2^N discrete voltage levels, with a voltage resolution of $V_{\text{res}} = (V_{\text{ADC}} - V_{\text{min}})/2^N$, where V_{ADC} is the maximum voltage that can be quantified, and V_{min} is minimum quantifiable voltage. The digitized voltage (which is normally represented by a binary code) is then

$$\text{ADC}_{\text{code}} = \text{round}[A_{\text{ADC}} \cdot (V_{\text{input}} - V_{\text{min}})], \quad (20)$$

for an input voltage of V_{input} , and where $A_{\text{ADC}} = V_{\text{res}}$ is the ADC gain. The digitization introduces quantization noise, modeled by the round function. It is assumed that the quantization error is uniformly distributed between -0.5 and $+0.5$ of the least significant bit and uncorrelated with the signal.

Ideally there should be an exact linear response between the input voltage and the corresponding digital code. However, the ADC introduces two nonlinearity errors: Integral Linearity Error (ILE) and Differential Linearity Error (DLE). Integral linearity error (Figure 5a) is the maximum deviation between the actual conversion digital code and the digital code expected from a straight line between minimum and maximum values. ILE is a measure of the straightness of the transfer function, and cannot be corrected by calibration. Differential linearity error (Figure 5b) arises if an increase (delta) in input voltage, V_{res} corresponding to exactly one digital increment, does not produce exactly one digital increment. Nonlinear gain in the ADC is modeled by a modified form of Konnik's model,² where the gain is a function of the input voltage:

$$A_{\text{ADC}}(V_{\text{input}}) = \left(\frac{1}{V_{\text{res}}}\right)^{1 - \left[\frac{V_{\text{input}} - V_{\text{min}}}{V_{\text{ADC}} - V_{\text{min}}}\right] \left[\frac{\log(\gamma_{\text{ADC}}/V_{\text{res}})}{\log(1/V_{\text{res}})} - 1\right]}. \quad (21)$$

This model starts linearly and introduces nonlinear behavior towards maximum voltage, compressing the input for $\gamma_{\text{ADC}} < 1$.

3. MODEL IMPLEMENTATION AND VALIDATION

3.1 Implementation

The original version of this model was implemented in Matlab by Konnik.² The present (modified) model was implemented in Python as part of the open source pyradi^{3,10} library and also in the C++ OSSIM⁴ simulation environment. Both implementations provide the facility to output intermediate step data for inspection and debugging. Some of these results are shown in Section 4. As a side note, beware of computer Poisson distribution generators: they break down at photon rate magnitudes (2×10^9 for the C++ Boost library, 64-bit Python Numpy issues a value error warning at 2×10^8).

3.2 Model validation

All models should be validated and verified prior to use. Techniques used include²⁵ comparison with all available data (physics/mathematical models, measurements, other models, etc.), the use of experts (models, reviews), internal and cross-model consistency checks (does it work the way it should?), and testing (parameter sensitivity and regression). Normally a balanced mix of techniques is used. Essentially, the model details and results must be in agreement with a preexisting knowledge base.

Validation is to confirm that a model reflects reality. This model is based on published information from first principle physics and mathematics, publications by established experts and peer reviewed papers. Jamesick,^{1,22} Kinch,¹⁶ Konnik²⁴ and others provide ample data and measurement results. It is reasonable to accept this model design is based on accepted and tested models. Verification is to confirm that the computer implementation performs the calculation accurately. The results shown in Section 4 demonstrate that the simulation results agree with expectations for both visual CCD and infrared CMOS sensors. Signal values, noise values and spatial values have the correct magnitudes and scale correctly from one block to the next. Some of the submodels in the CMOS mode is not yet extensively tested, but the bulk of the CMOS model shares a large commonality with the CCD model. The remaining work is to characterize a commercially available sensor and verify the model predictions against the measured results.

4. EXAMPLE RESULTS

4.1 Objective

The objective with this section is to demonstrate the model's application to two sensors: (1) to evaluate a visual band sensor's SNR under twilight conditions, (2) a MWIR sensor viewing a fighter aircraft against a cloudy sky background, and (3) a MWIR sensor viewing two scenes.

The results are presented in Figures 6 and 8, showing the signal in various locations along the processing chain as subfigures. The meaning of each picture and its corresponding location in the signal processing chain are provided as caption to the subfigure. The following description applies equally to both figures.

Figure 6a shows the input photon rate irradiance image, with no photon noise present. Figure 6b shows the spatial PRNU (Section 2.4.1). The effect of this PRNU on the image is shown in Figure 6c; note the noise in the image at all signal levels. Figure 6d shows the number of electrons in the charge well, *prior to well saturation*, accounting for the detector area and integration time. Figure 6e shows the dark current in the sensor, together with the dark current noise. This noise has a Poisson distribution with a number of high value outliers (Section 2.4.5). Figure 6f shows the dark current spatial nonuniformity, which follows a lognormal distribution. Figure 6g shows the electrons in the charge well after the dark noise is added and the well is saturated at maximum capacity. Figure 6h shows the sense node voltage (on the charge well), decreasing from the reference voltage at low light levels, towards zero for higher light levels. Figure 6i shows the source follower noise, while Figure 6j shows the signal plus the source follower noise. Figure 6k shows the signal after the DCS. Finally, Figure 6l shows the image in digital numbers at the output of the ADC.

4.2 Low-light sensor performance evaluation

The visual CCD sensor has the following characteristics: visual spectral range CCD technology with 5 μm pitch, unity fill factor, PRNU of 0.01% RMS, quantum efficiency of 0.8, well capacity 20k e^- , sense node gain of 5×10^{-5} V/e, integration time 0.01 s, white noise density of 1.5×10^{-8} V/ $\sqrt{\text{Hz}}$, flicker noise corner 1 MHz, operating temperature 300 K, and 12-bit ADC. More detail is available in the pyradi example notebook 09b.¹⁰

The input to the sensor is a stepwise graded 'image' providing 40 different photon flux levels from zero to a maximum of 25 lux (a relatively bright twilight). The signal images at some locations along the signal flow are displayed in Figure 6.

The input photon rate irradiance on the detector is around 1×10^{17} q/(s.m²), representing the twilight conditions. The PRNU shows a peak-to-peak variation of about 6% around 1.0, corresponding to the 1% RMS PRNU. The effect of this PRNU on the image is shown in Figure 6c; note the noise in the image at all signal levels. Figure 6d shows that the maximum signal corresponds with the pixel's well capacity. This is because the integration time was selected for maximum well fill at maximum irradiance. This was done to cover the full sensor dynamic range to support subsequent analysis. Note the Poisson noise distribution with a number of high value outliers in Figure 6e (Section 2.4.5). Figure 6f shows the dark current spatial nonuniformity, which follows a lognormal distribution. It is evident that the few very large dark noise peaks are about 10 times smaller than the charge well capacity, but the bulk of the dark noise counts are about 100 times smaller than the well capacity. This value is later order-of-magnitude verified in Figure 7d. The charge well clipping is shown in Figure 6g but in this case the maximum signal is just at the limit of well capacity and clipping is not clearly evident. Finally, Figure 6l shows the image in digital numbers at the output of the ADC. The noise in the image and the maximum digital number count (4096, corresponding to the 12-bit ADC).

Each step in the stepwise graded image provides a different irradiance level, and hence it can be used to calculate various signal-related characteristics. All the graphs in Figure 7 show effects such as charge well saturation and nonlinearity. Figure 7a shows the digital number output for various irradiance levels. Note the charge well saturation effect at maximum levels. The graph also shows a nonlinearity in the response (not a perfect straight line). Figure 7b shows the signal transfer function (output divided by the input) versus irradiance. It is evident that the signal transfer function is not a constant (i.e., nonlinear). At lower irradiance levels noise becomes visible, compared to the signal. Figure 7c shows the RMS noise as a function of irradiance. Note that under saturated well conditions the noise drops, whereas under low irradiance conditions the noise is constant. The dominating noise source is fixed pattern noise, because it is proportional to the input irradiance. Figure 7d

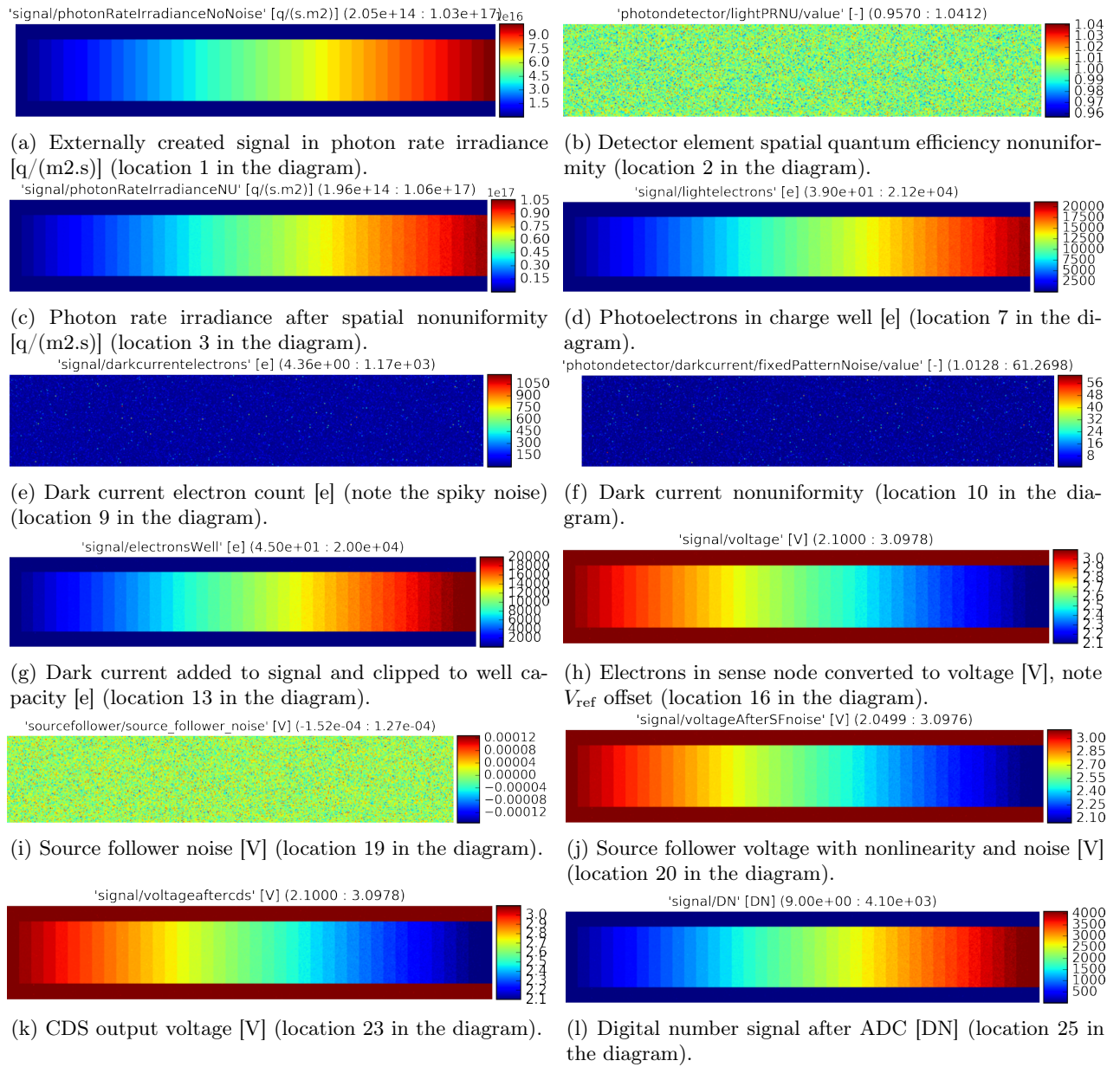


Figure 6: Linear wedge image at various locations.

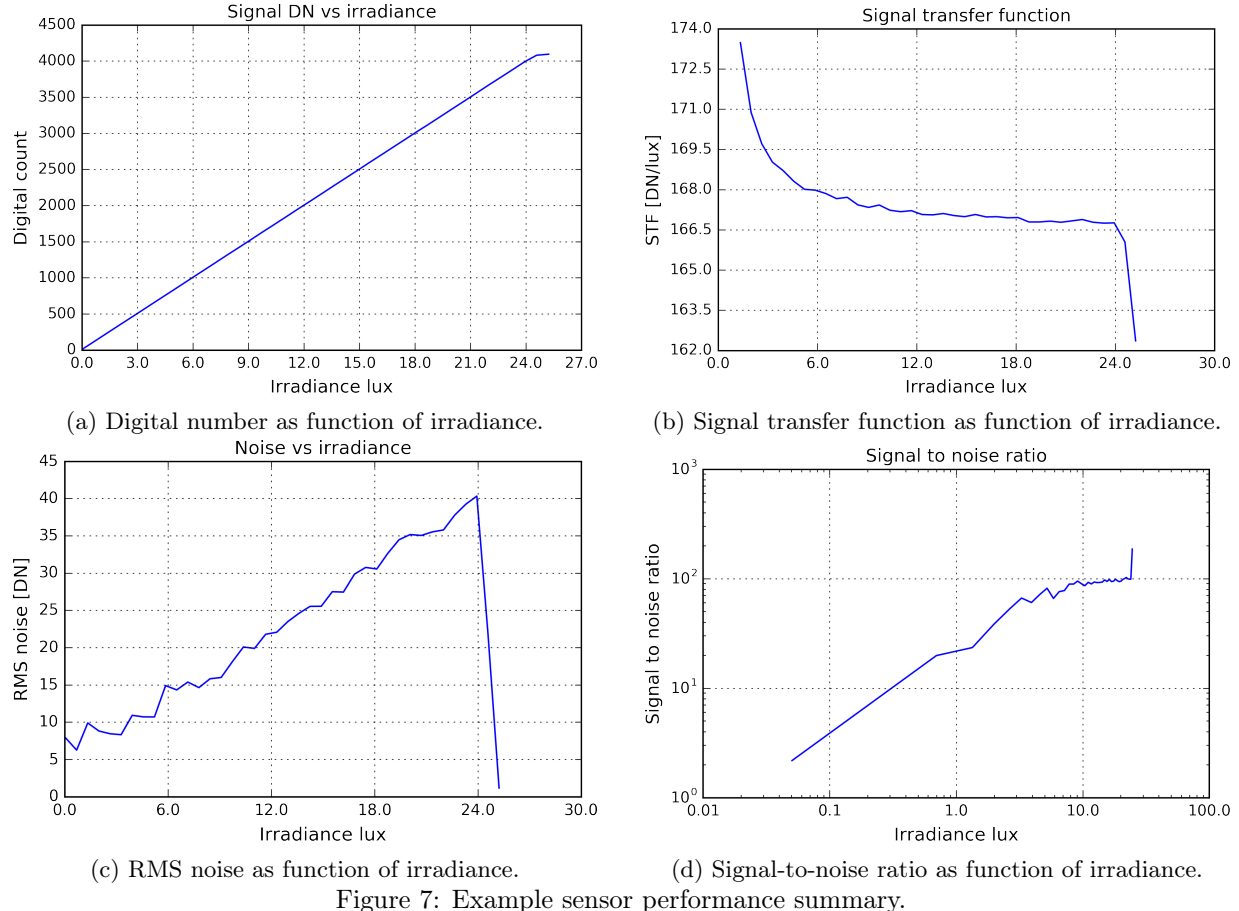


Figure 7: Example sensor performance summary.

shows the SNR as a function of irradiance. The shape of this curve agrees very well with similar results for real cameras. For this camera the SNR is quite low at dark current levels, rising to about 100 at high signal levels.

4.3 MWIR sensor performance evaluation

4.3.1 Fighter aircraft

The aircraft has a high contrast plume (700 K, CO₂) signature against the warm (≈ 340 K) fuselage and cold cloudy sky (270 K). The pictures in Figure 8 correspond with the locations for the pictures shown in Figure 6. The following sensor characteristics were used: 3.2 f-number optics, assuming optics perfectly matched to the detector cold stop. The optics and sensor window both have a transmittance of 0.8 and temperature of 313 K. The detector is a HgCdTe 3.5–4.7 μm device operating at 80 K, 12 μm pitch, 0.95 fill factor, PRNU corrected by nonuniformity correction to 0.002% RMS, quantum efficiency of 0.5, well capacity 3.2×10^6 e⁻, sense node gain of 3.1×10^{-7} V/e, integration time 0.005 s, white noise density of 1.5×10^{-8} V/ $\sqrt{\text{Hz}}$, flicker noise corner 1 MHz, and 14-bit ADC.

The integration time was set to view the fuselage at a well fill of 50%, with the result that the hot plume saturates in the image. The short integration time results in a wide dynamic range (scene minimum to scene maximum), but at this low sensitivity, the sensor noise is not visible.

From Figure 8a it is evident that the infrared signal has a 25% well fill minimum value (digital number is 4340, out of a 14-bit range of 16384), arising from the flux from the minimum scene, path radiance and hot optics. This large minimum flux value fills up the charge well but carries no information and leads to a reduction in the number of digital number bits on the target.¹⁵

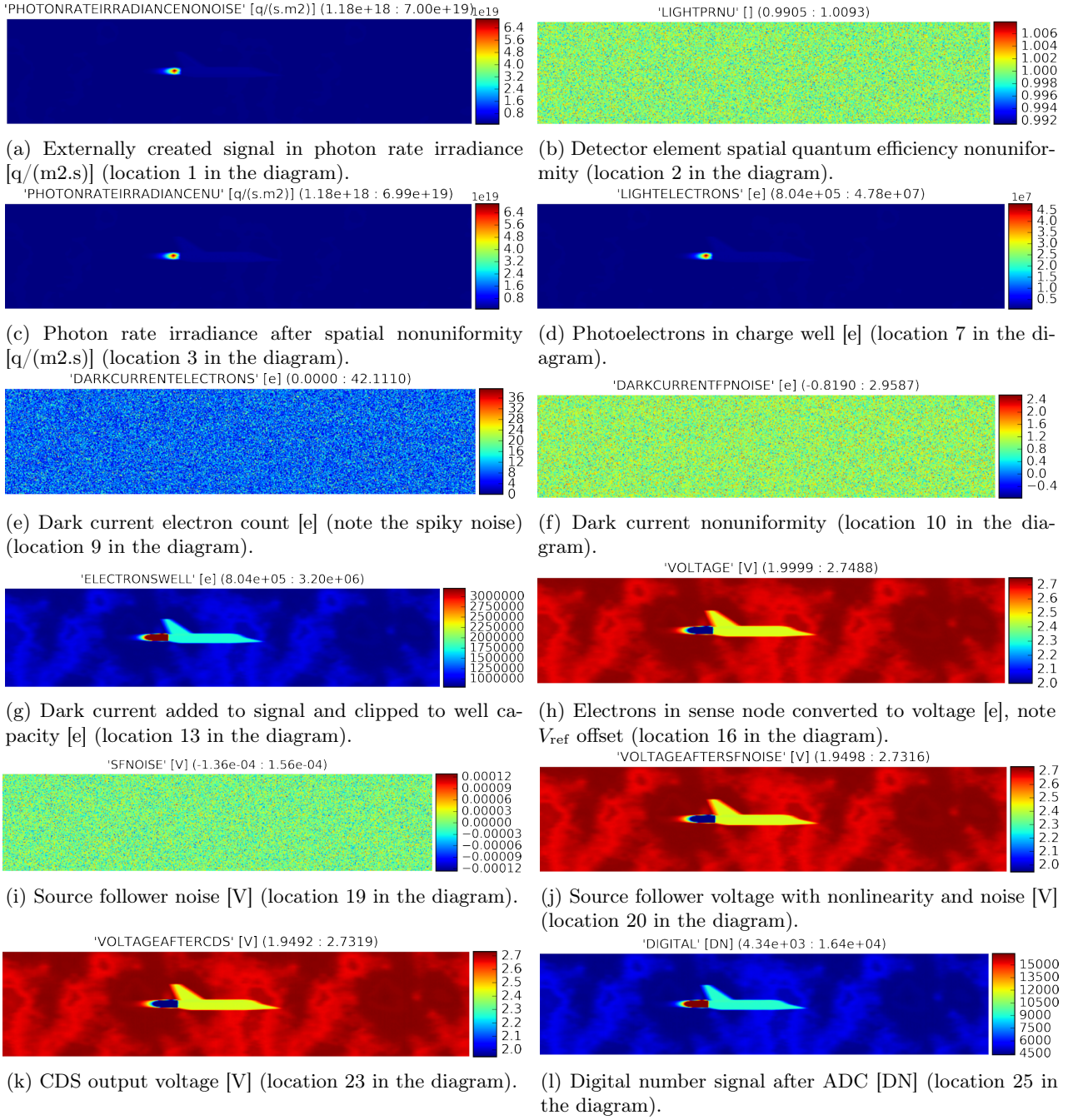


Figure 8: MWIR picture of a fighter aircraft.

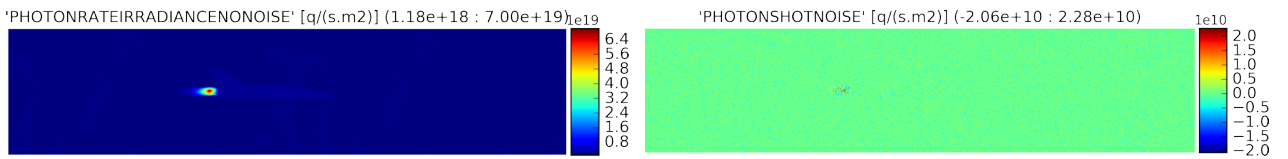
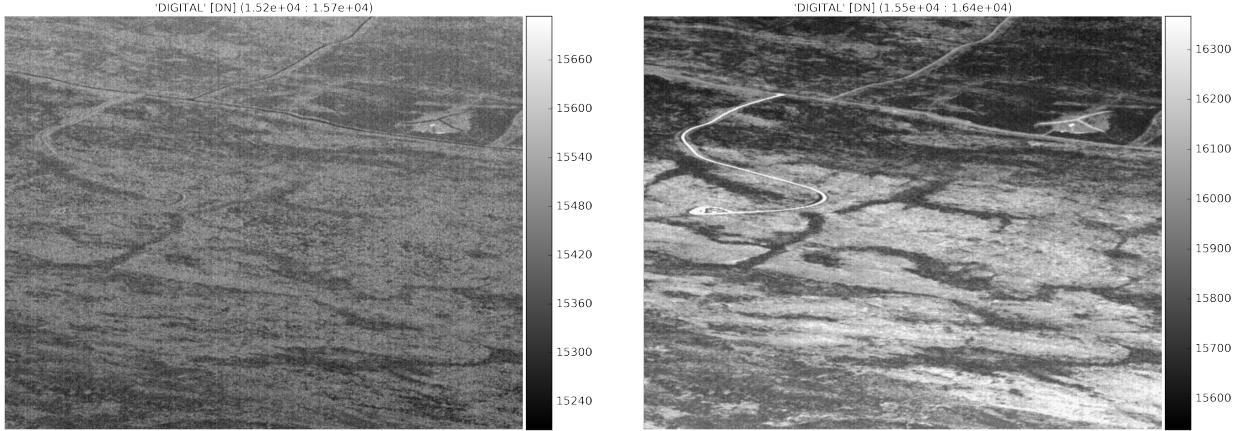


Figure 9: Confirmation of photon rate noise in location 2 in the diagram.



(a) Low contrast scene: 07:30 in the morning with mean temperature 13.6°C and 7.6°C dynamic range (location 25 in the diagram).
(b) Intermediate contrast scene: 15:00 in the afternoon with mean temperature 25.5°C and 22.5°C dynamic range (location 25 in the diagram).

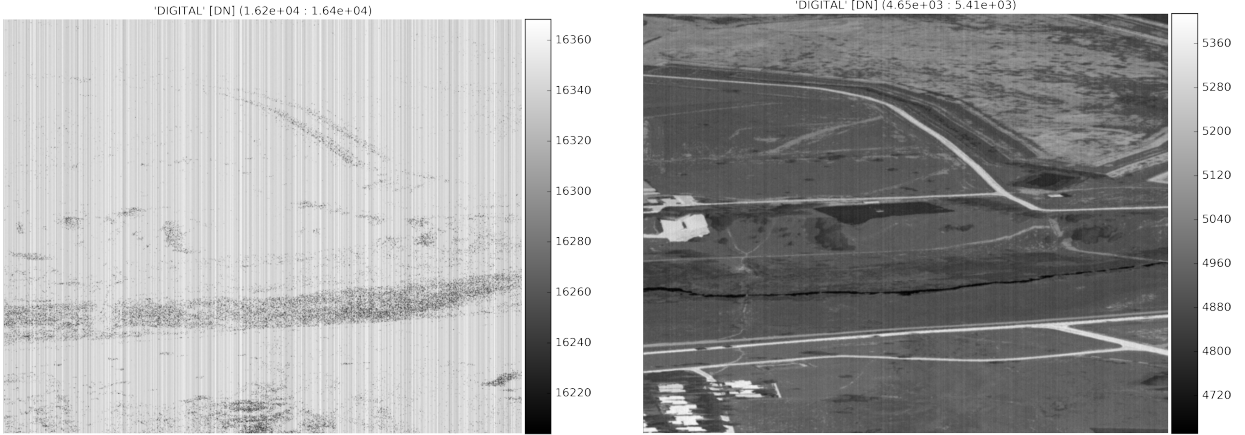
Figure 10: A simulated coastal vegetation scene as viewed through a 20°C optics with 64% transmittance.

Figure 8l shows that the minimum well fill is about 30%. Figure 8d indicates that the plume pixels create many more photoelectrons than be stored in the charge well. These large numbers will be clipped in the charge well (Figure 8g) and lead to saturation in the image (Figure 8l). Figure 9 shows the signal irradiance and the photon shot noise per pixel. Note that magnitude of the photon noise is higher in the plume than elsewhere, because photon noise Poisson variance is equal to the mean.

4.3.2 Observing low contrast terrain scenes

Figure 10 shows the same coastal vegetation scene in the morning (07:30) and afternoon (15:00) played through the sensor model (modeled in C++ in OSSIM⁴). The low dynamic range scene requires the relatively long integration time of 19 ms. As a result of the long integration time and very small dynamic range in the image, the sensor noise is clearly visible. In this early morning example the relatively cool scene is viewed through warm optics, and hence has a considerable well fill (94%) and small scene dynamic range ($\sigma=0.33\%$ of well fill). The scene has a 318 digital number peak-to-peak variation ($\sigma=53.7$ digital numbers) on top of a constant of 15430 digital numbers. At these low signals, even a small residual nonuniformity creates a huge digital number variation as compared to the scene dynamic range. In this case a 0.2% residual nonuniformity leads to $0.002 \times 15430 = 30$ digital numbers, and the resulting image has a rms-signal-to-rms-noise ratio of 1.7, which clearly is quite poor. This important observation leads to the recommendation that nonuniformity correction for infrared sensors should be performed at well fill levels corresponding to the minimum and maximum in the scene, not to fixed percentage levels in the charge well.

Figure 11 shows another scene also at 07:30 and 15:00. In this case the morning picture is well saturated (on purpose) to show the structured FPN. In this case the noise has column structure, but it is a simple matter to extend the model to other structures.



(a) Rural terrain with some industry, very low contrast 07:30, sensor set to very small dynamic range (location 25 in the diagram).
(b) Rural terrain with some industry, moderate contrast 15:00 (location 25 in the diagram).

Figure 11: An urban scene as viewed through a 20°C optics with 64% transmittance.

5. CONCLUSION

The paper provided an overview of an existing model²⁴ expanded for use in the SWIR and MWIR bands. The modular design of the model allows easy implementation in any computer language, such as Python³ and C++ as part of a larger simulation system. The high-level model is developed from first principles and supports a large number of variables to model a variety of sensors. It was shown that, given realistic input data, the model can provide realistic results.

A model is never quite finished. This model can be adapted to suit the characteristics of a specific sensor. This generic model can be extended to (1) allow for more than one serial readout (each block with its own source follower and CDS spatial behavior, (2) improved models for more sense node configurations, (3) and an improved voltage-dependent sensor node capacitor model.

ACKNOWLEDGMENTS

The work reported here is based on a model described by Konnik²⁴ and work performed at Airbus DS Optronics and Denel Dynamics, both located in Irene, South Africa. Thanks to Hannie van den Bergh whose testing pointed out that shot noise must also be calculated on the electrons in the charge well (Section 2.4.4).

REFERENCES

- [1] Janesick, J. R., *Photon Transfer*, Vol. PM170, SPIE (2007) [doi: 10.1117/3.725073].
- [2] Konnik, M. and Welsh, J., “High-level numerical simulations of noise in CCD and CMOS photosensors: review and tutorial,” *arXiv:1412.4031 [astro-ph.IM]* arXiv:1412.4031 (2014).
- [3] Pyradi team, “Pyradi Radiometry Python Toolkit,” <https://github.com/NelisW/pyradi>.
- [4] Willers, M. S. and Willers, C. J., “Key considerations in infrared simulations of the missile-aircraft engagement,” *Proc. SPIE* **8543**, 85430N (2012) [doi: 10.1117/12.974801].
- [5] Murray, S., “What’s new with CMOS imaging arrays,” http://www.pha.jhu.edu/~stephan/CAS_seminar/Slides/s2011-03-22_CMOS_real.pdf.
- [6] Analog Devices, “Integrated Solutions for CCD Signal Processing,” http://www.analog.com/library/analogdialogue/archives/32-1/signal_pro.html.
- [7] Chih-Cheng Hsieh and Chung-Yu Wu and Far-Wen Jih and Tai-Ping Sun, “Focal-Plane-Arrays and CMOS Readout Techniques of Infrared Imaging Systems,” *IEEE Trans. Circuits and Systems for Video Technology* **7**(4) (August 1997).

- [8] Willers, C. J., Willers, M. S., and Lapierre, F. D., "Signature modelling and radiometric rendering equations in infrared scene simulation systems," *Proc. SPIE* **8187**, 81870R (2011) [doi: 10.1117/12.903352].
- [9] Willers, C. J., *Electro-Optical System Analysis and Design: A Radiometry Perspective*, Vol. PM236, SPIE Press, Bellingham, WA (2013).
- [10] Cornelius J Willers, "Computational Optical Radiometry Notebook 09b Staring Array Detectors," <https://github.com/NelisW/ComputationalRadiometry>.
- [11] Wikipedia, "Fano noise," https://en.wikipedia.org/wiki/Fano_noise.
- [12] Wikipedia, "Fano factor," https://en.wikipedia.org/wiki/Fano_factor.
- [13] Physics Stackexchange, "Why isn't the variance of Fano noise proportional to the number of photon arrival?," <http://physics.stackexchange.com/questions/15923>.
- [14] Black, W. T., *In Situ Calibration of Nonuniformity in Infrared Staring and Modulated Systems*, PhD thesis, University of Arizona (2014).
- [15] Willers, C. J. and Goss, T. M., "MWIR sensor well fill: sources, effects and mitigation," *Proc. SPIE* **10036** (2016).
- [16] Kinch, M. A., *Fundamentals of Infrared Detector Materials*, SPIE Press, Bellingham, WA (2007).
- [17] Widenhorn, R., Blouke, M. M., Weber, A., Rest, A., and Bodegom, E., "Temperature dependence dark current in a CCD," *Proc. SPIE* **4669** (2002).
- [18] Raptor Photonics, "Ninox White Paper," <http://www.raptorphotonics.com/wp-content/uploads/2015/10/Ninox-White-Paper-Draft5.pdf>.
- [19] Wikipedia, "Johnson–Nyquist noise," https://en.wikipedia.org/wiki/Johnson–Nyquist_noise.
- [20] Fossum, E. R., "Charge Transfer Noise and Lag in CMOS Active Pixel Sensors," *IEEE Workshop on Charge-Coupled Devices and Advanced Image Sensors* (2003).
- [21] Tian, H., *Noise analysis in CMOS image sensors*, PhD thesis, Applied Physics, Stanford (2000).
- [22] Janesick, J. R., *Scientific Charge-Coupled Devices*, Vol. PM83, SPIE (2001).
- [23] Gamal, A. E., Fowler, B., Min, H., and Liu, X., "Modeling and estimation of FPN components in CMOS image sensors," *Proc. SPIE* **3301**, 168–177 (1998).
- [24] Konnik, M. V. and Welsh, J. S., "On numerical simulation of high-speed CCD/CMOS-based wavefront sensors in adaptive optics," *Proc. SPIE* **8149** (2011) [doi: 10.1117/12.892667].
- [25] Willers, C. J. and Wheeler, M. S., "The validation of models in an imaging infrared simulation," *IEEE International Microwave and Optoelectronics Conference (IMOC)* (2007).